Available online at www.sciencedirect.com
ScienceDirect
Trans. Nonferrous Met. Soc. China 35(2025) 91−104
Transactions of Nonferrous Metals Society of China
www.tnmsc.cn

Processing, microstructure, and mechanical properties of wire arc additively-manufactured AZ91 magnesium alloy using cold arc process

Bai-hao CAI[1,2], Ji-kang FAN[1,2], Jie LI[1,2], Dong-qing YANG[1,2], Yong PENG[1,2], Ke-hong WANG[1,2]

1. Key Laboratory of Controlled Arc Intelligent Additive Technology, Ministry of Industry and Information Technology, Nanjing University of Science and Technology, Nanjing 210094, China;
2. School of Materials Science and Engineering, Nanjing University of Science and Technology, Nanjing 210094, China

Received 19 September 2023; accepted 20 March 2024

Abstract: Thin walls of an AZ91 magnesium alloy with fine equiaxed grains were fabricated via cold arc-based wire arc additive manufacturing (CA-WAAM), and the droplet transfer behaviours, microstructures, and mechanical properties were investigated. The results showed that the cold arc process reduced splashing at the moment of liquid bridge breakage and effectively shortened the droplet transfer period. The microstructures of the deposited samples exhibited layered characteristics with alternating distributions of coarse and fine grains. During layer-by-layer deposition, the β-phase precipitated and grew preferentially along grain boundaries, while the fine η-Al_8Mn_5 phase was dispersed in the α-Mg matrix. The mechanical properties of the CA-WAAM deposited sample showed isotropic characteristics. The ultimate tensile strength and elongation in the building direction (BD) were 282.7 MPa and 14.2%, respectively. The microhardness values of the deposited parts were relatively uniform, with an average value of HV 69.6.

Key words: AZ91 magnesium alloy; droplet transfer; microstructure; mechanical properties; cold arc process

1 Introduction

Magnesium alloys, as the lightest structural metallic materials in the practical engineering applications, have specific advantages, such as high specific strength, low density, good vibration resistance, and superior electromagnetic shielding performance [1−3]. This approach has enormous potential for application in the fields of aerospace, automotive, and medical instruments [4,5].

The material preparation process is an important reason hindering the further development of high-performance magnesium alloys [6]. The traditional manufacturing methods for magnesium alloy parts mainly include deformation processes (hot rolling, hot extrusion, and forging) and casting processes [7]. However, the deformation process of the magnesium alloy parts always leads to long preparation time, high costs, partial oxidation, and difficulty in forming structural parts with complex geometric shapes [8]. During the casting process, various problems, such as coarse grains, shrinkage cavities, and poor mechanical properties, can easily occur [9]. In addition, the hexagonal closed packing (HCP) structures of magnesium alloys result in poor cold deformation processability and ductility [10]. With the increasing demand for low energy consumption, high efficiency, and high performance in the modern manufacturing industry, the selection of the magnesium alloy manufacturing process is increasingly valued [11].

Corresponding author: Ji-kang FAN, Tel: +86-17705192919, E-mail: fanjk@njust.edu.cn;
Ke-hong WANG, Tel: +86-13951698524, E-mail: wkh1602@126.com
https://doi.org/10.1016/S1003-6326(24)66667-7

Wire arc additive manufacturing (WAAM) is a wire-based directional energy deposition (DED) method in which an electric arc is used as a heat source to melt wires and fabricate parts in a layer-by-layer manner [12,13]. Compared to selective laser melting (SLM) [14], WAAM has several advantages, including a high deposition rate (reaching 4 kg/h), high material utilization, and no risk of magnesium powder explosion. Therefore, WAAM has distinct benefits in the rapid manufacturing of large and intricate magnesium alloy components.

Currently, AZ series magnesium alloys are widely used due to their superior specific strength and low cost. GUO et al [15] successfully obtained an AZ31 thin wall with equiaxed grains using gas tungsten arc welding (WAAM-GTAW). The research indicated that the pulse frequency can affect the oscillations of the weld pool and the cooling rate, which leads to grain refinement. The ultimate tensile strength can reach 260 MPa at the optimal parameters. CAI et al [16] reported that the overall mechanical properties of AZ91D magnesium alloys deposited by WAAM-GTAW are greater than those of cast samples. Among the various wire-arc additive manufacturing methods, GMAW is an efficient method due to its high deposition rate and inexpensive equipment [17]. However, the low density, low melting point, and low boiling point of magnesium alloys can lead to various issues, such as spatter, grain coarsening, oxidation, and evaporation, during the WAAM process [18−20]. Consequently, researchers have increasingly focused on reducing the heat input during the arc deposition process of magnesium alloys [21,22]. YANG et al [23] investigated the relationship between the microstructures and mechanical properties of an AZ31 component deposited using the WAAM-cold metal transfer (CMT) method. The tensile properties exhibit noticeable anisotropic characteristics, and the microstructures mainly consist of α-Mg matrix, β-$Mg_{17}Al_{12}$, and some dispersed η-Al_8Mn_5 phases. CAO et al [24] demonstrated that ultrasonic frequency pulsed (UFP) arc is beneficial to reducing porosity, refining grains, and improving mechanical properties. In addition, the scholars applied UFP to the WAAM of magnesium alloys. Furthermore, several researchers have reported that the interlayer temperature significantly influences the formability, microstructural evolution, and mechanical properties of WAAM magnesium alloys [25−27].

As an advanced arc welding technology, the cold arc (CA) process is a controlled short-circuit metal transfer mode that minimizes heat input and precisely controls melt droplet transfer during the WAAM process, contributing to the additive manufacturing of heat-sensitive materials [28]. Compared with the CMT process, the CA process does not require mechanical control of the wire feeding system [29]. WANG et al [30] successfully applied alloy coatings to the surface of an AZ61 magnesium alloy via the pulsed-cold arc (P-CA) process, resulting in a coating structure with a uniform composition and excellent performance. However, the CA-WAAM process for AZ91 magnesium alloy compositions has rarely been reported.

In this study, a single-pass multilayer component of an AZ91 magnesium alloy with fine equiaxed grains is fabricated by CA-WAAM. The processability, microstructures, and mechanical properties of the CA-WAAM samples are investigated. Furthermore, the evolution of the microstructure and its influence on the mechanical properties are discussed in detail. In this study, an effective method for fabricating large magnesium alloy components with complex geometries is provided.

2 Experimental

2.1 Experimental setup and manufacturing process

A 1.2-mm-diameter AZ91 wire produced by Viktor Magnesium Alloy Technology Co., Ltd. (Henan, China) was used as the filler metal, and its chemical composition is listed in Table 1. AZ91 plates with dimensions of 450 mm × 150 mm × 10 mm were employed as substrates for the deposition. Before manufacturing, the base metal was polished, cleaned, degreased with acetone, and preheated to approximately 200 °C.

Table 1 Chemical composition of AZ91 wire (wt.%)

Al	Zn	Mn	Mg
8.62	0.55	0.33	Bal.

The fabrication of AZ91 thin wall was conducted using a CA–WAAM system, as depicted in Fig. 1(a). The system consisted of a six-axis robot

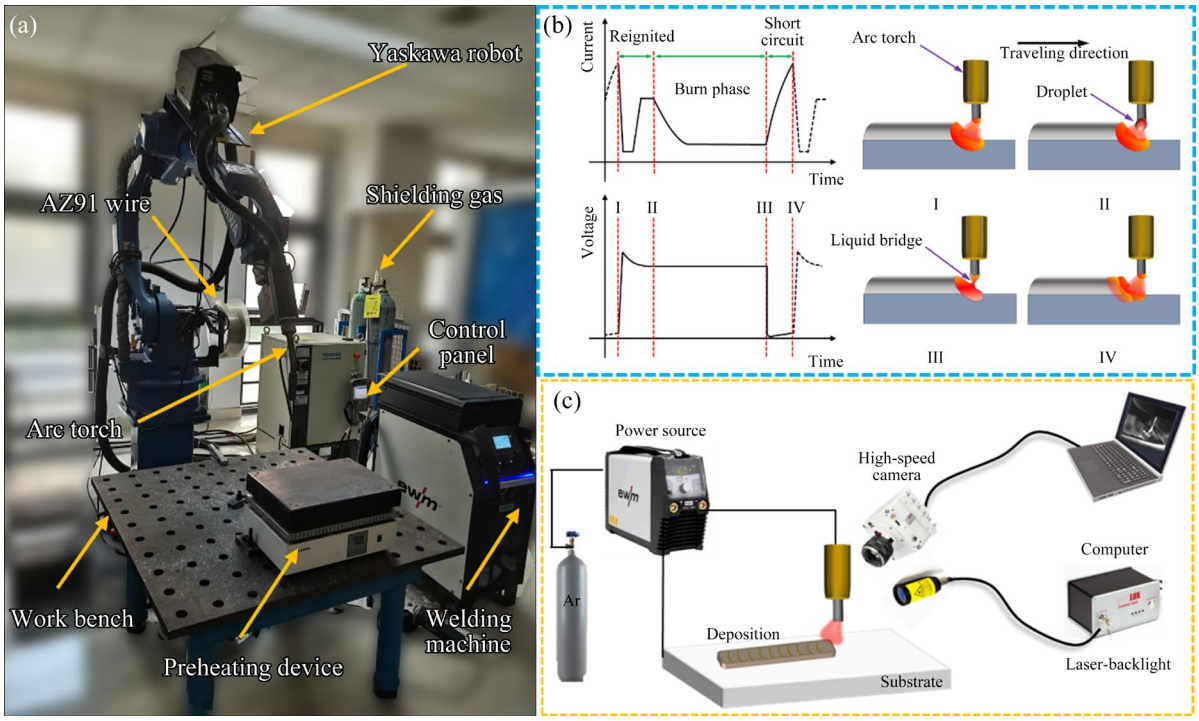

Fig. 1 Schematic diagram of CA-WAAM process for thin wall component of AZ91 Mg

(YASKAWA, YRC1000), a cold arc welding machine (EWM, PC300), a wire feeder, a heating unit and an argon gas transport system. A unidirectional travelling strategy was used in the experiment, where the platform was kept stationary, and the wire was melted onto the previously melted layer as the welding torch moved. The manufacturing parameters obtained after conducting preliminary trials are presented in Table 2. An arc torch swing system with a swing length of 10 mm and a swing width of 5 mm was used to ensure that the deposited wall was effectively formed. In cold arc mode, precise control of the current and voltage was implemented to stabilize the droplet transfer. At the moment of arc ignition after short circuiting, the current dramatically decreased to ensure smooth disconnection of the liquid bridge (I in Fig. 1(b)). The current increased slightly to promote rapid melting of the wire to form droplets (II in Fig. 1(b)). Subsequently, the current gradually decreased and was maintained at a low level to control the droplet size. The arc remained in a steady burn phase until the droplets contacted the molten pool, and the current increased sharply to allow the pinch effect (III in Fig. 1(b)). After arc ignition, the peak current decreased in a dynamically controllable manner (IV in Fig. 1(b)).

Table 2 Deposition parameters used in experimental process

Deposition parameter	Value
Current/A	170
Voltage/V	17
Wire feed speed/(m·min^{-1})	8
Travelling speed/(cm·min^{-1})	24
Swing wide/mm	5
Interlayer temperature/°C	200
Gas flow rate/(L·min^{-1})	18

A smooth transition of the droplets was critical to ensuring that the final part had good shape and performance. As shown in Fig. 1(c), the transfer behaviours of the droplets were observed and recorded using a Phantom® VEO VWO410L high-speed camera with a frame rate of 4000 frames per second. A filter with a wavelength of 640 nm and a background laser system were used to improve image contrast.

2.2 Experiment

The samples for analysis were taken from the top, middle, and bottom regions of the structural components shown in Fig. 2(a). The metallographic

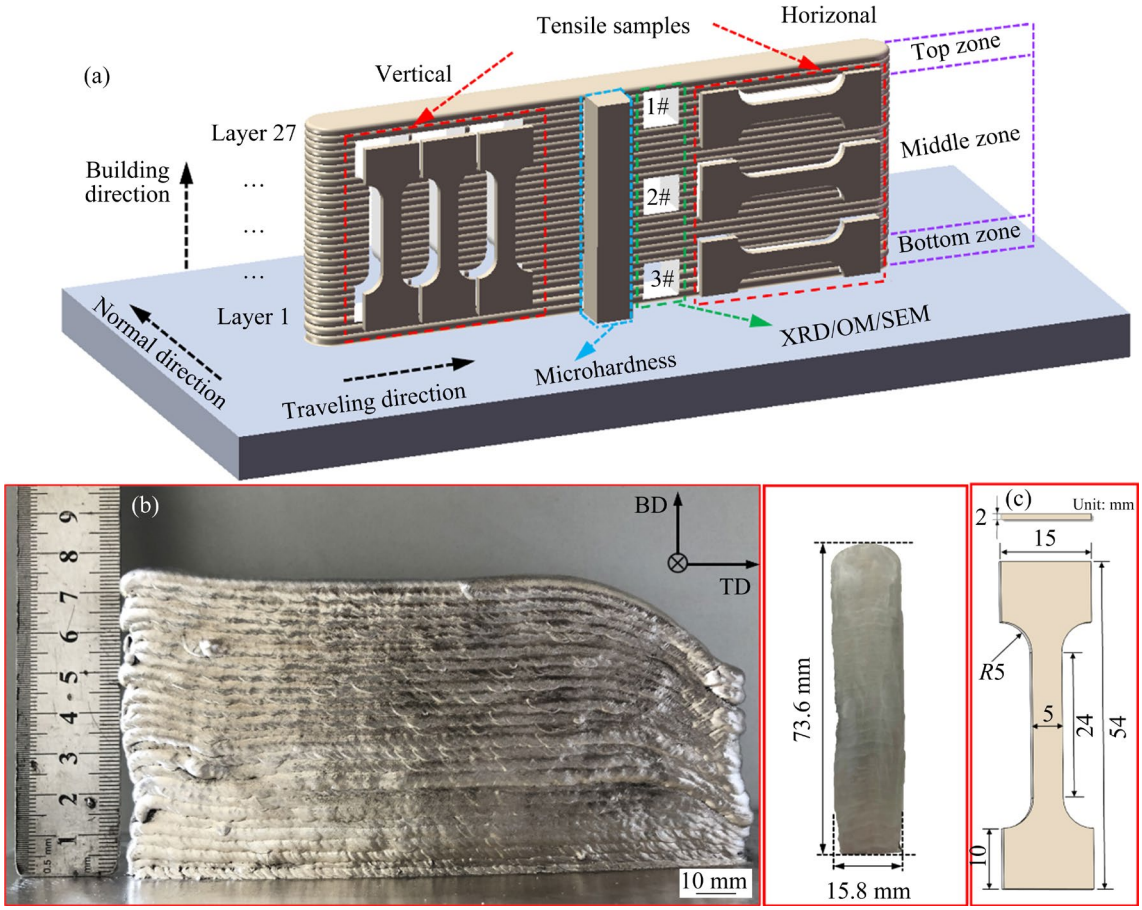

Fig. 2 Schematic diagrams indicating cutting position and test surface of metallographic, XRD, and microhardness test samples (a); Macro morphology and cross-section of AZ91 thin wall (b); Tensile test specimens from AZ91 thin wall (c)

specimens were finely ground to 3000 grit with silicon carbide sandpaper, polished with a diamond suspension and etched using a solution of 1 g of oxalic acid, 3 mL of acetic acid, and 60 mL of distilled water. The macro morphology and micromorphology features were observed via optical microscopy (OM; Olympus OLS4000), and the microstructures and elemental distributions were analyzed by scanning electron microscopy (SEM; FEI Quanta 250F) and energy dispersive X-ray spectroscopy (EDS). The phase compositions were analyzed by X-ray diffraction (XRD; Bruker-AXD D8 Advance X). XRD was performed using Cu K_α radiation at 40 kV and 40 mA and an angle range of 20°−80°.

The microhardness distribution along the building direction was measured using a Vickers hardness tester (HVS-1000Z) with a load of 200 g and a retention time of 15 s. Tensile samples were cut along the vertical and horizontal directions at different deposition heights with the dimensions shown in Fig. 2(c), and tensile tests (MOBEL1186) were performed at a constant loading rate of 1 mm/min at room temperature. The fracture morphology was examined by scanning electron microscopy.

3 Results and discussion

3.1 Deposition quality

The macroscopic morphology and cross-section of a single-pass multilayer of AZ91 magnesium alloy fabricated with CA-WAAM are shown in Fig. 2(b). Twenty-seven layers were required to form the deposit with dimensions of 150 mm (length) × 15.5 mm (width) × 73.5 mm (height), and the average layer thickness was approximately 2.7 mm. Furthermore, the deposit showed distinct layer-by-layer characteristics. There were no obvious defects, such as cracks or incomplete fusion, in the component, except for the collapse at the end positions. This crack was attributed to poor heat dissipation at that stage, where heat buildup promoted the flow of liquid metal.

3.2 Droplet transfer behavior

Figure 3 illustrates the metal transfer dynamic process of the CA mode in one cycle. The typical short-circuit transition period of the CA-WAAM process was 31 ms and consisted of three phases: burn phase, short-circuit phase, and arc reignition phase. At t_0, as the current dramatically decreased, the arc reignited smoothly between the metal wire and the molten pool. Due to the smaller discharge area of the metal wire compared to the surface of the base metal, an inverted funnel-shaped arc was formed. Subsequently, the arc burned and melted the metal wire, resulting in the formation of a droplet at the tip. The lower heat input during this process led to the droplet exhibiting as a relatively regular spherical shape. The occurrence of spatter coming from the molten pool at t_0+2.5 ms could be attributed to the violent fluctuation and instability of the molten pool caused by the strong arc force generated during the peak stage of the pulse current. Previous research indicated that the spatter volume generated by arc forces was the smallest among the various sources of splash generation [31].

Interval from t_0+2.5 ms to t_0+27 ms in Fig. 3 represented the arc burn phase. During this phase, the current remained at a low level, and the droplet grew in the axial direction of the wire. As the metal wire was fed, the distance between the droplet and the molten pool decreased. The droplet was stretched in the axial direction due to gravity, electromagnetic force, and surface tension. This stretching made it easier for the droplet to contact the molten pool and enter the short-circuit transition phase. As a result, the arc burning time was shortened, and the size of the melt droplet was reduced. Notably, at t_0+19 ms, the molten droplet exhibited deviation from the axis of the metal wire and moved towards the direction of travel. This phenomenon could be attributed to the high evaporation pressure and low density of magnesium, which resulted in the generation of a substantial amount of metal vapor on the surface of the droplet and within the molten pool at the elevated temperature of the arc [32]. The recoil force generated by evaporation caused the droplet to move away from the wire axis, leading to the transfer of repelled metal. This phenomenon was frequently observed in the pure MIG additive manufacturing of magnesium alloys and degraded significantly the forming quality of parts [33]. Furthermore, the image processing software ImageJ was used to measure the maximum droplet diameter, which was approximately 1.5 times the wire diameter before the droplet entered the molten pool.

At t_0+27 ms, the short-circuit transition phase began, and a liquid bridge was formed between the wire and molten pool. The electromagnetic force was an important factor for accelerating the necking of liquid bridges [34]. At t_0+31 ms, a small neck was formed between the wire and the molten pool, after which the droplet transfer was facilitated by the combined effects of surface tension and electromagnetic force. Ultimately, the arc was reignited, and the cycle was repeated. In the present case, the arc energy of the CA-WAAM deposition process was effectively controlled, resulting in decreased droplet transfer period, elimination of spatters, and improved droplet transition stability.

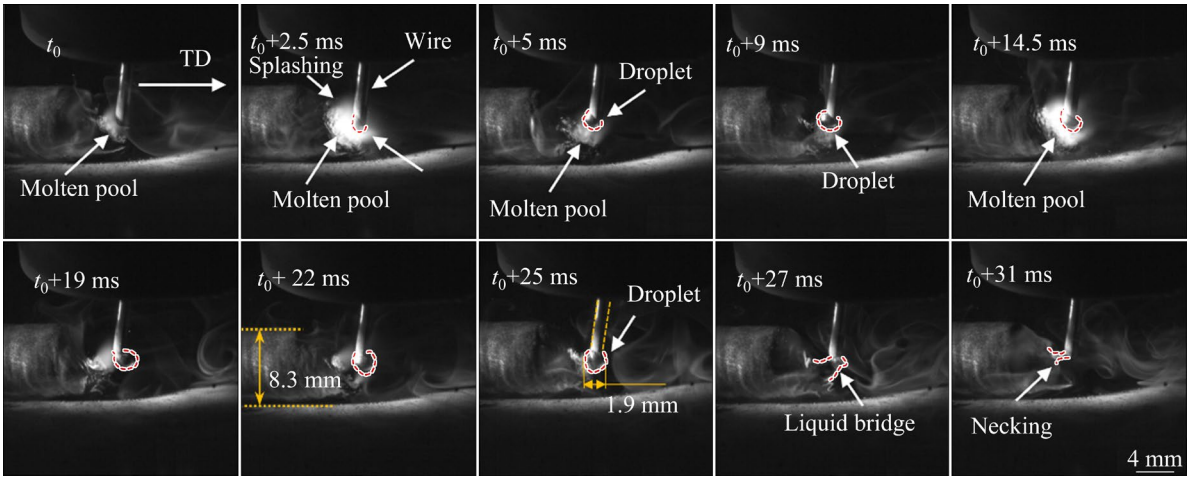

Fig. 3 One entire droplet transfer cycle during deposition

3.3 Microstructure

The XRD analysis results of the AZ91 Mg alloy sample fabricated by CA-WAAM are shown in Fig. 4. The phase composition was characterized by the presence of α-Mg and a small amount of β-$Mg_{17}Al_{12}$. The diffraction peaks of η-Al_8Mn_5 were not identified due to the low content of this phase, which deviated from the findings of other studies [35].

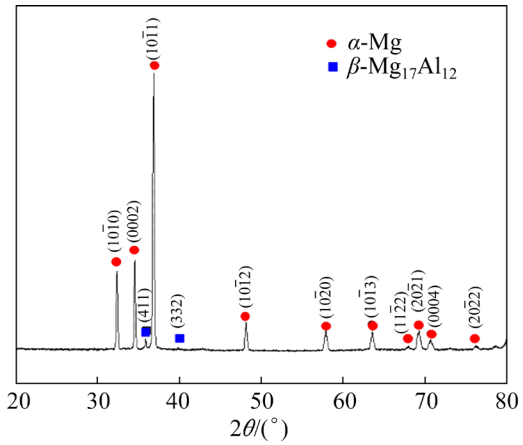

Fig. 4 XRD patterns of deposited sample

The phase formation of the AZ91 Mg alloy (Mg−9.5Al−0.5Zn−0.3Mn) was illustrated using an equilibrium phase diagram and Scheil−Gulliver solidification path, which were calculated by the thermodynamic software JMatPro (Fig. 5). As the temperature of the molten pool decreased, the Al_8Mn_5 phase and primary α-Mg precipitated from the liquid at 627 °C and 600 °C, respectively. Subsequently, the Al_8Mn_5 phase transformed into the $Al_{11}Mn_4$ phase at 540 °C, which transformed into the Al_4Mn phase at 407 °C. During gradual cooling, the Al diffused in the α-Mg phase solid solution, and the $Mg_{17}Al_{12}$ phase precipitated from the supersaturated solid solution α-Mg phase at 372 °C. However, the cooling in the CA-WAAM process for magnesium alloys was a nonequilibrium solidification process. Due to the low content of Mn (0.3%) in the deposited parts, the Al_8Mn_5 phase failed to sufficiently precipitate from the liquid phase at high cooling rates, resulting in a low content. Therefore, the nonequilibrium microstructure of the AZ91 Mg alloy component fabricated by CA-WAAM technology should primarily consist of α-Mg phase, $Mg_{17}Al_{12}$ phase, and a negligible amount of precipitated Al−Mn phase.

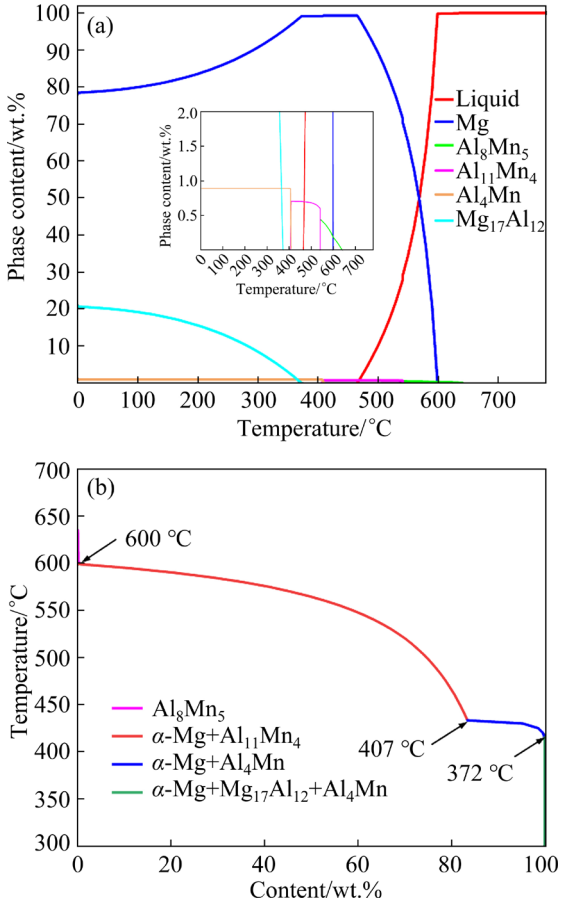

Fig. 5 Equilibrium phase diagram (a) and Scheil−Gulliver solidification path of AZ91 alloy calculated using thermodynamic software JMatPro (b)

The microstructures of different regions of the thin-wall longitudinal section (*XOZ* plane) of the AZ91 magnesium alloy deposited by the CA-WAAM process are shown in Fig. 6. All regions of the sample consisted of equiaxed grains, and the microstructure exhibited layered characteristics with alternating distributions of coarse grains and fine grains due to the multiple thermal cycles of the layer-by-layer manufacturing process. The microstructure at the top of the former deposited layer was remelted by the heat source during the deposition of the subsequent layers. The boundary of the molten pool was in direct contact with the former deposited layer or substrate during solidification, leading to greater undercooling and heterogeneous nucleation of the contact surface, and thus increasing the tendency to form fine equiaxed crystals. However, the microstructure of the former deposited layer near the fusion line was reheated to a high temperature, causing diffusion of the alloying elements in the matrix and resulting in

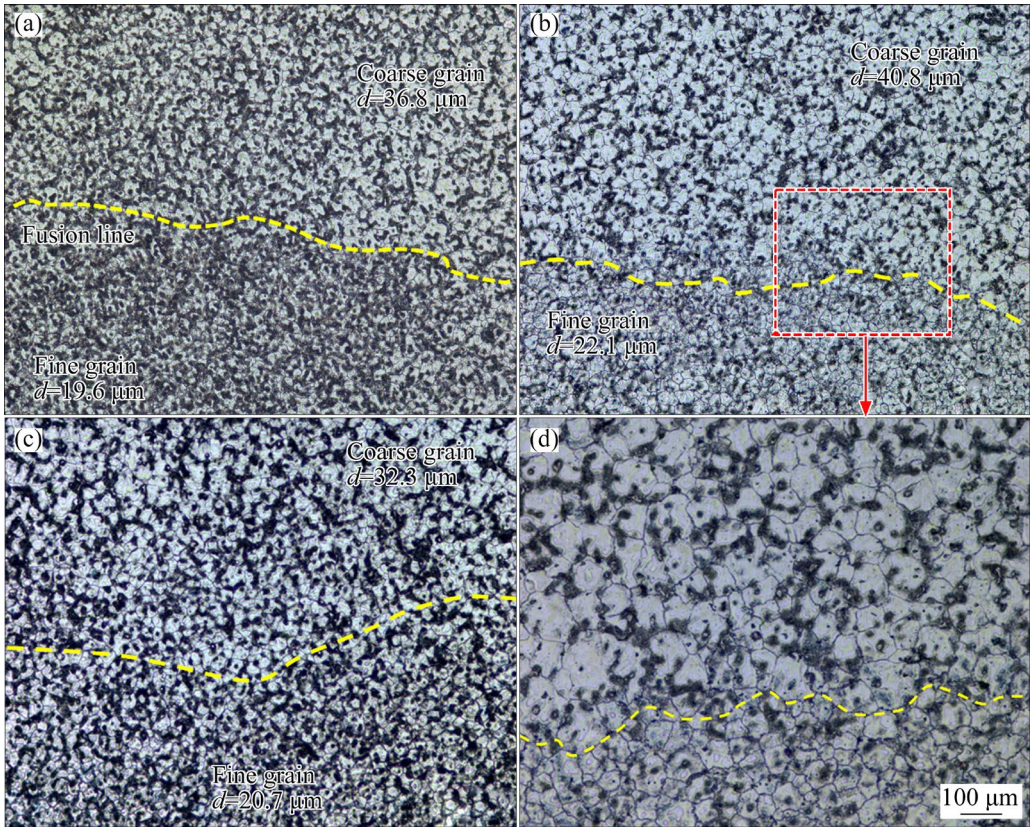

Fig. 6 Optical micrographs of AZ91 magnesium alloy fabricated by CA-WAAM: (a) Microstructure of bottom layer; (b) Microstructure of middle layer; (c) Microstructure of upper layer; (d) Details of microstructure in (b)

grain coarsening. Figures 6(a−c) show that the average sizes of coarse and fine grains in the middle area of sample were 40.8 and 22.1 μm, respectively, which were larger than those in the bottom and upper areas of the sample. This phenomenon could be attributed to better heat dissipation conditions near the substrate in the bottom area and fewer thermal cycles experienced in the top area. The grain size near the fusion line in the middle zone was calculated using Nano Measurer software, and the maximum and minimum grain sizes were 48.7 and 6.95 μm, respectively. It has been widely recognized that fine grains not only shorten the dislocation slip range and make the deformation more dispersed and homogeneous but also activate non-basal slip systems in magnesium alloys and lead to grain boundary sliding, thereby improving the plastic deformation capacity of magnesium alloys.

Figure 7 shows the SEM images and EDS results of different regions for the deposited AZ91 magnesium alloy. The microstructure consisted mainly of primary α-Mg matrix, supersaturated eutectic α-Mg solid solution, β-$Mg_{17}Al_{12}$ phase, and a small amount of η-Al_8Mn_5 phase. The EDS results indicated that the contents of Mg and Al in the dark grey α-Mg matrix were 94.1 at.% and 5.9 at.%, respectively (Fig. 7(i)), while were approximately 60.7 at.% and 39.3 at.%, respectively (Fig. 7(f)) in the eutectic phase. The eutectic phase contained more Al than the α-Mg matrix. During the solidification process, the solute Al did not evenly diffuse when the liquid phase was transformed into primary α-Mg, resulting in its enrichment in the unsolidified liquid phase. Subsequently, in the eutectic reaction, the primary α-Mg was surrounded by precipitated β phases, leading to the formation of a network of eutectic structures distributed along the grain boundaries. The bottom and middle zones exhibited coarser β-$Mg_{17}Al_{12}$ phases, and more submicron β phases precipitated along the grain boundaries. This result could be attributed to the preferential precipitation and growth of the β-phase along the grain boundaries due to the multiple thermal cycles during layer-by-layer deposition. Furthermore, the EDS results in Figs. 7(h, j) revealed the presence of fine η-Al_8Mn_5 phase dispersed in the α-Mg matrix.

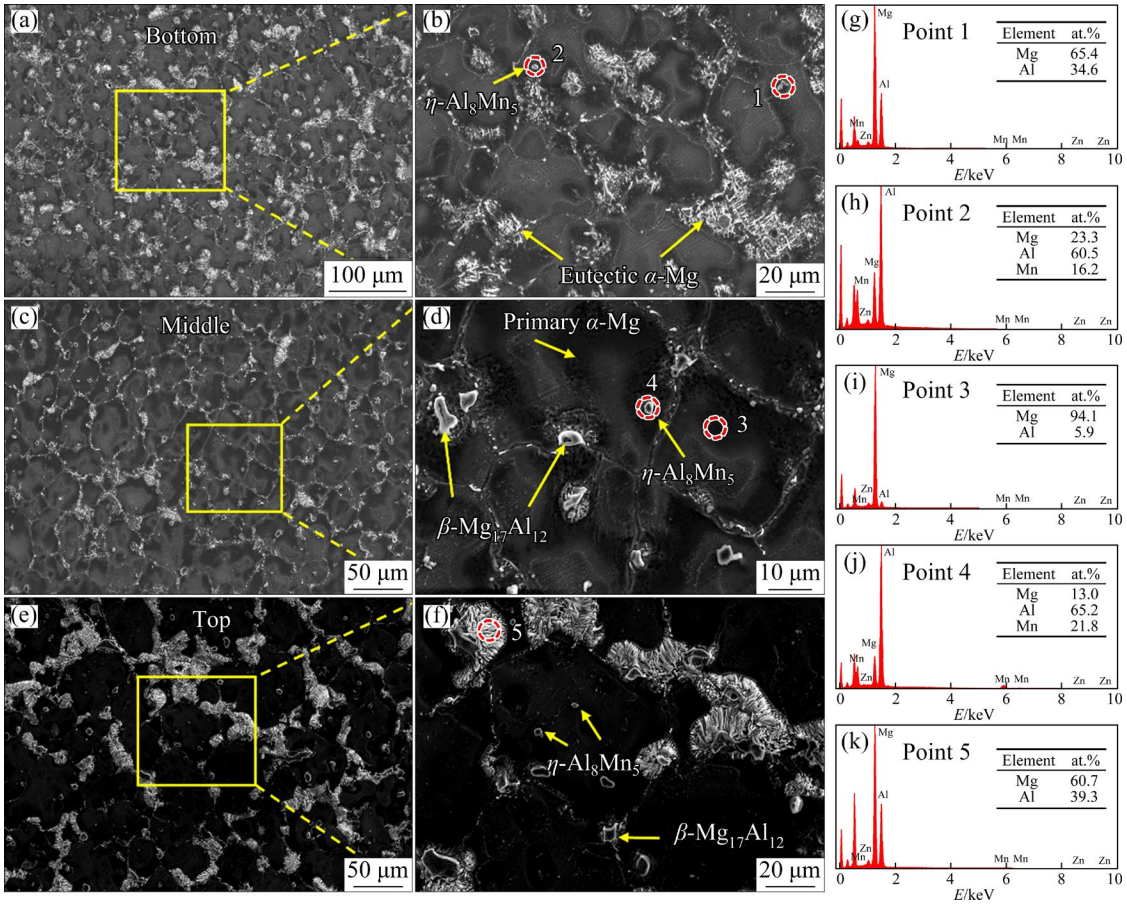

Fig. 7 SEM images with EDS results for different regions of AZ91 magnesium alloy deposited part: (a, b) Bottom zone; (c, d) Middle zone; (e, f) Upper zone; (g−k) EDS patterns corresponding to Points 1, 2, 3, 4 and 5

The EDS elemental analysis results of the microstructure in the middle region of the deposited part are shown in Fig. 8. Figures 8(b, e) illustrate the distribution characteristics of major elements, such as Mg, Al, Mn, and Zn. Al and Mn were mainly concentrated in the precipitated phase. The short-bar β phase and granular β phase precipitated discontinuously along the grain boundaries. Based on the previous analysis, it was evident that the CA-WAAM process consistently maintained a low heat input during the deposition process. Additionally, the high thermal conductivity of magnesium alloys led to a high cooling rate during the solidification process of the molten pool. Consequently, the Al in the α-Mg matrix became supersaturated, and fine and dispersed precipitates were discontinuously formed within the grains due to the effects of multiple thermal cycles during subsequent deposition. Figure 8(f) shows the line scanning results for the precipitated phase in the α-Mg matrix. The content of Mg significantly decreased from the primary α-Mg phase to the precipitated phase, while the contents of Al and Mn increased. The content of Al in the precipitated phase was greater than that of Mg, suggesting that the precipitated phase was the Al−Mn phase. Furthermore, Fig. 8(g) showed a high content of Mn in the eutectic β-$Mg_{17}Al_{12}$ phase. Scholars previously indicated that the η-Al_8Mn_5 phase could serve as an effective nucleation site for the β-$Mg_{17}Al_{12}$ phase [36].

3.4 Mechanical properties

3.4.1 Microhardness

Figure 9 shows the microhardness distributions of the different zones on the longitudinal section (*XZ* plane) of the AZ91 magnesium alloy samples deposited using CA-WAAM. The hardness was measured at intervals of 0.5 mm. Based on the observation of the microstructure, the grain structure of the AZ91 component consisted of fine equiaxed crystals, resulting in minimal variation in the hardness distribution across each sample. The average hardness in the bottom zone was HV 68.1,

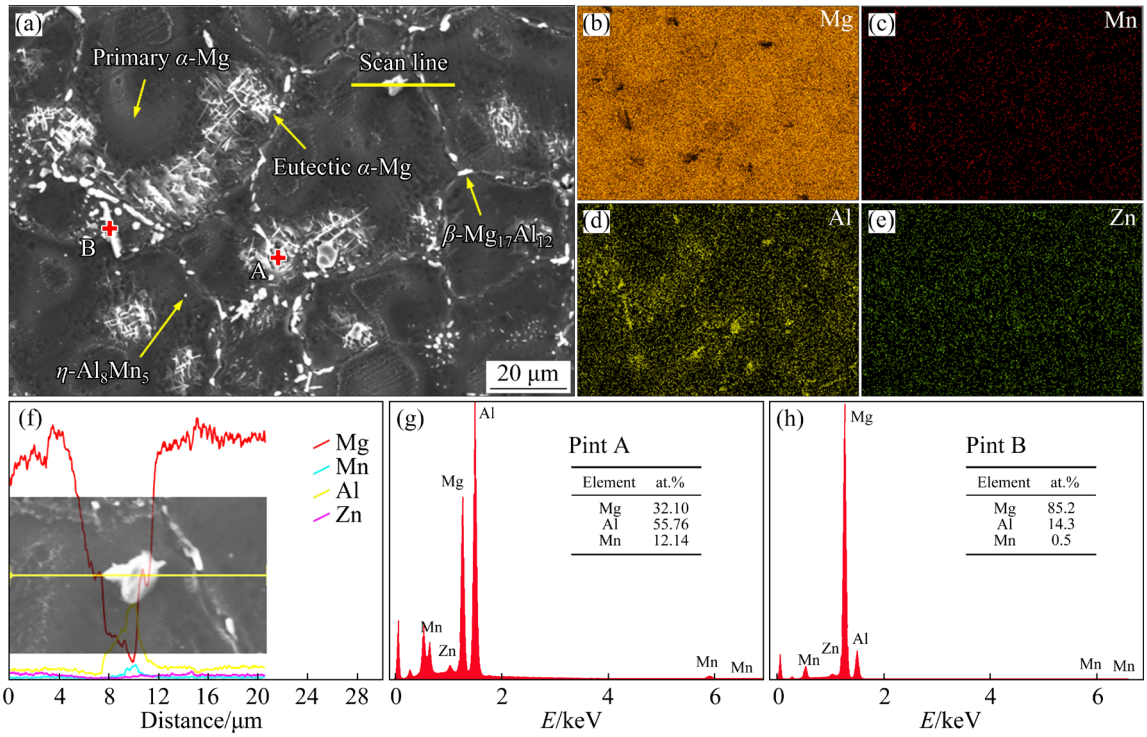

Fig. 8 EDS analysis results of AZ91 deposited component: (a) SEM image; (b−e) Elemental distribution maps of Mg, Mn, Al and Zn; (f) Line scanning analysis result in (a); (g, h) EDS results of Points A and B

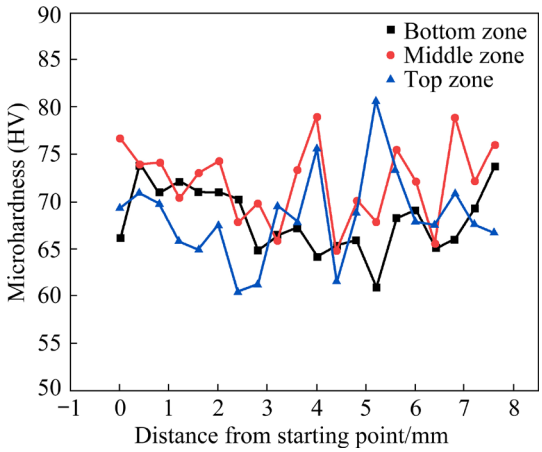

Fig. 9 Microhardness distribution of AZ91 thin wall in longitudinal section (*XZ* plane)

which was slightly lower than that in the middle zone. The hardness of the middle zone fluctuated due to the layer characteristic distribution of the microstructure, with an average value of HV 72.2. The average value in the top zone was HV 68.6. The uniformity of the microhardness indicated that grain size, rather than the distribution of precipitated phases, was the primary factor influencing hardness.

3.4.2 Tensile properties and fracture morphology

To investigate the anisotropy in the tensile properties of the thin wall specimens, tensile tests were conducted at various locations. The results are presented in Fig. 10, indicating that the tensile properties in the travelling direction were slightly lower than those in the building direction. The CA-WAAM AZ91 samples exhibited an ultimate tensile strength (UTS) of 282.7 MPa and an elongation (EL) of 14.2% along the building direction, which were higher than the values of 271.6 MPa and 11.3%, respectively, along the travelling direction. However, the yield strength (YS) along the building direction was 134.7 MPa, which was lower than the yield strength of 140 MPa in the travelling direction. Scholars have previously identified two main factors contributing to the lower yield strength in the building direction. First, numerous soft oriented grains (with Schmid factors greater than 0.4) were prone to slip in the sedimentary layer [37]; Second, the layered structure contained more small-angle grain boundaries (grain boundaries with orientations less than 10°) that minimally impacted dislocation motion during deformation [38]. The lower UTS and EL values of the tensile specimen in the travelling direction could be attributed to the presence of microcracks in the intergranular eutectic

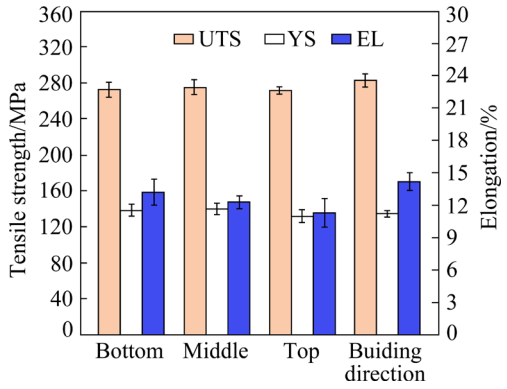

Fig. 10 Tensile properties of specimens in different regions

region perpendicular to the travelling direction, while the inner-layer fusion line in the horizontal direction was not conducive to the plasticity of the specimen due to the oscillation of the arc [39]. Furthermore, the UTS and EL values of the horizontal specimens at different heights from the substrate exhibited relatively similar values. To measure the degree of anisotropy in the tensile properties of the AZ91-deposited walls, an index was calculated according to Eq. (1) [40]:

$$\delta_X = \frac{X_{\max} - X_{\min}}{X_{\max}} \times 100\% \quad (1)$$

where X_{max} and X_{min} are the maximum and minimum values in the building direction and travelling direction, respectively, and δ_X is the performance index. According to Table 3, the calculated δ_{UTS}, δ_{YS} and δ_{EL} values of the AZ91-deposited wall were 3.9%, 3.7%, and 20.4%, respectively. The results indicated that the tensile properties of the material were isotropic. In contrast, the tensile properties of AZ91 magnesium alloys fabricated by different methods are summarized in Table 3. The CA-WAAM components of the AZ91 Mg alloy exhibited superior tensile properties compared to those of the die-cast AZ91 Mg alloy (230 MPa, 160 MPa, and 3%; ASTM standard B94—07), except for yield strength, which could be attributed to finer grain size and distribution of fine β-Mg17Al12 phase at the grain boundary. Furthermore, the AZ91 single-pass multilayer parts in this study had higher tensile strengths than the AZ91 magnesium alloys deposited by the WAAM-CMT [16] and WAAM-GTAW [41].

Figure 11 shows the fracture morphology of the tensile specimens at different positions on the AZ91 magnesium alloy components. The results demonstrated that the tensile specimens primarily exhibited a ductile–brittle hybrid fracture pattern characterized by numerous dimples, ductile tearing ridges, and discontinuous quasicleavage. Furthermore, noticeable small secondary cracks were observed on the fracture surface due to the stress concentration caused by the brittle β-$Mg_{17}Al_{12}$ phase and micropores under tensile stress. As shown in Fig. 11(d), fine secondary phase particles were distributed on the fracture surface. The finely diffusely distributed β phases precipitated in the α-Mg matrix not only hindered the extension of cracks but also exerted a pinning effect on dislocation movement, resulting in transgranular fracture. Conversely, secondary phases precipitated along the grain boundaries were prone to intergranular fracture under tensile stress, thereby reducing the plasticity. Additionally, the fracture morphologies of the specimens in the building direction exhibited more ductile tearing ridges and fewer stream patterns (Fig. 11(h)). Moreover, additional microcracks were observed on the fracture surfaces of the transverse specimens.

Table 3 Comparisons of tensile properties of AZ91 Mg alloy fabricated by different methods

Method	Direction	Ultimate tensile strength/MPa	Yield strength/MPa	Elongation/%
CA-WAAM (This study)	Building direction	282.7±7.2	134.7±3.6	14.2±0.8
	Travel direction	273.9±3.6	136.8±6.5	12.2±0.9
Die casting (ASTM standard B94—07)		230	160	3
WAAM-GTAW [16]	Building direction	243.5	107.7	11.5
	Travel direction	243.7	113.3	11.9
WAAM-CMT [40]	Building direction	250.3±2.6		17.5±1.6
	Travel direction	245.2±1.0		16.3±1.0

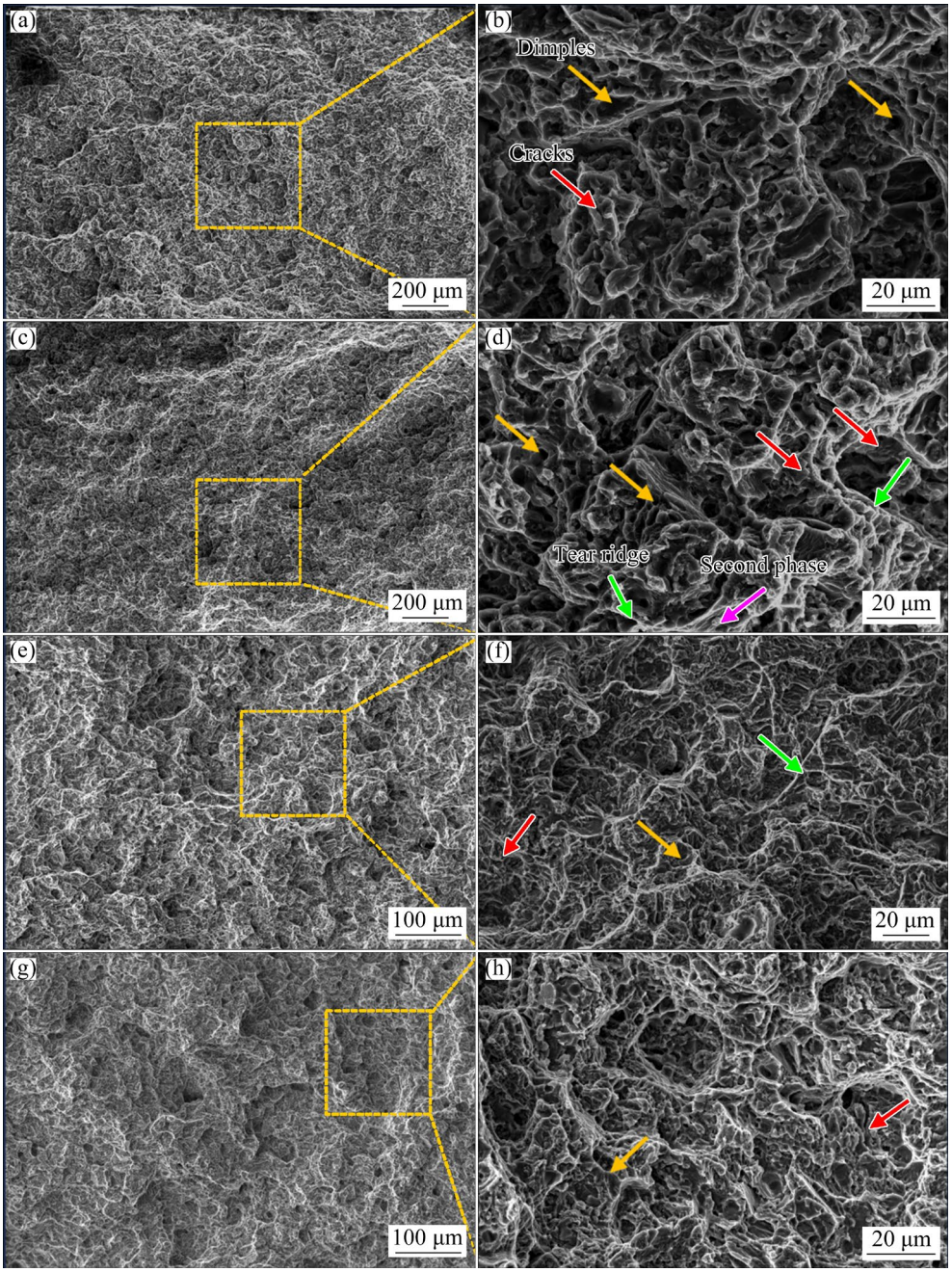

Fig. 11 Fracture morphologies of AZ91 tensile samples: (a, b) Top area; (c, d) Middle area; (e, f) Bottom area; (g, h) Vertical direction

4 Conclusions

(1) The CA-WAAM process of a magnesium alloy successfully prevented splashing during liquid bridge fracture by reducing the energy peak of the short-circuit transition. The droplet transfer period was significantly shortened, with an average value of 31 ms. The molten droplets deviated from the wire axis under the influence of the recoil force of droplet evaporation, thereby compromising the stability of the arc.

(2) The AZ91 structural part fabricated using the CA-WAAM process consisted of equiaxed grains, and the microstructure was characterized by layers of alternating coarse and fine grains due to the occurrence of multiple thermal cycles. The average sizes of the fine- and coarse-grained regions in the central area of the structure were approximately 22.1 and 40.8 μm, respectively. The precipitated phases in the AZ91 sample included the β-$Mg_{17}Al_{12}$ phase and a small amount of the

η-Al_8Mn_5 phase, with the β phase being smaller in the upper zone.

(3) The hardness distributions in different regions of the deposited parts exhibited uniformity, with an average hardness value of HV 69.6. The tensile properties of the CA-WAAM deposited components demonstrated isotropy in both the building and travelling directions. The average ultimate tensile strength (UTS), yield strength (YS), and elongation (EL) of the specimens in the travelling direction were 272.9 MPa, 136.8 MPa, and 12.2%, respectively. Moreover, the tensile fracture exhibited ductile–brittle hybrid fracture characteristics.

CRediT authorship contribution statement

Bai-hao CAI: Methodology, Investigation, Visualization, Writing − Original draft; **Ji-kang FAN:** Conceptualization, Supervision, Writing − Review & editing; **Jie LI:** Methodology, Investigation; **Dong-qing YANG:** Supervision, Writing – Review & editing; **Yong PENG:** Supervision, Investigation; **Ke-hong WANG:** Funding acquisition, Project administration.

Declaration of competing interest

The authors declare that they have no known competing financial interests or personal relationships that could have appeared to influence the work reported in this paper.

Acknowledgments

This work was supported by the National Natural Science Foundation of China (No. 51805265), and the Fundamental Research Funds for the Central Universities, China (No. 30922010921).

References

[1] YAN Fu-yao, CHEN Bao-feng, YAO Jia-wei, ZHANG Dan-li, YAN M F, ZHANG Yan-xiang. Characterization of microstructure and corrosion properties of AZ91D magnesium alloy surface treated by coating-nitriding [J]. Journal of Materials Research and Technology, 2021, 14: 1559−1568.

[2] CHEN Li-wen, ZHAO Yu-hong, HOU Hua, ZHANG Tian, LIANG Jian-quan, LI Mu-xi, LI Jing. Development of AZ91D magnesium alloy-graphene nanoplatelets composites using thixomolding process [J]. Journal of Alloys and Compounds, 2019, 778: 359−374.

[3] LUO Huan, LI Jian-bo, YE Jun-liu, TAN Jun, RASHAD Muhammad, CHEN Xian-hua, HAN Sheng-li, ZHENG Kai-hong, ZHAO Tian-tian, PAN Fu-sheng. Effect of Ti−6Al−4V particle reinforcements on mechanical properties of Mg−9Al−1Zn alloy [J]. Transactions of Nonferrous Metals Society of China, 2022, 32(10): 3238−3249.

[4] XIE He, WU Guo-hua, ZHANG Xiao-long, LI Zhong-quan, LIU Wen-cai, ZHANG Liang, SUN Bao-de. Microstructural evolution and mechanical performance of cast Mg−3Nd−0.2Zn−0.5Zr alloy with Y additions [J]. Transactions of Nonferrous Metals Society of China, 2022, 32(10): 3222−3237.

[5] LIAO Jin-sun, YAMAMOTO N, NAKATA K. Gas tungsten arc welding of fine-grained AZ31B magnesium alloys made by powder metallurgy[J]. Materials & Design, 2014, 56: 460−467.

[6] WEI Kai-wen, GAO Ming, WANG Ze-min, ZENG Xiao-yan. Effect of energy input on formability, microstructure and mechanical properties of selective laser melted AZ91D magnesium alloy [J]. Materials Science and Engineering A, 2014, 611: 212−222.

[7] FANG Xue-wei, YANG Jian-nan, WANG Shuai-peng, WANG Chuan-bin, HUANG Ke, LI Hao-nan, LU Bing-heng. Additive manufacturing of high performance AZ31 magnesium alloy with full equiaxed grains: Microstructure, mechanical property, and electromechanical corrosion performance [J]. Journal of Materials Processing Technology, 2022, 300: 117430.

[8] WEI Kai-wen, WANG Ze-min, ZENG Xiao-yan. Influence of element vaporization on formability, composition, microstructure, and mechanical performance of the selective laser melted Mg−Zn−Zr components [J]. Materials Letters, 2015, 156: 187−190.

[9] YAN Qian, SONG Bo, SHI Yu-sheng. Comparative study of performance comparison of AlSi10Mg alloy prepared by selective laser melting and casting [J]. Journal of Materials Science & Technology, 2020, 41: 199−208.

[10] XU Nan, REN Zi-ke, FAN Yue, GU Bo-kun, SHEN Jun, SONG Qi-ning, ZHAO Jian-hua, BAO Ye-feng. Microstructural evolution and mechanical properties of cooling medium assistant friction stir processed AZ31B Mg alloy [J]. Transactions of Nonferrous Metals Society of China, 2023, 33(6): 1729−1741.

[11] ZHANG Xuan-chang, SHI Hai-long, WANG Xiao-jun, ZHANG Shuai, LUAN Peng, HU Xiao-shi, XU Chao. Processing, microstructure, and mechanical behavior of AZ31 magnesium alloy fabricated by electron beam additive manufacturing [J]. Journal of Alloys and Compounds, 2023, 938:168567.

[12] CAO Qian-hui, ZENG Cai-you, CAI Xin-yi, ZHANG Ruize, WANG Fu-de, WANG Hai-bo, ZHANG Yu, QI Bo-jin, CONG Bao-qiang. High-strength Mg−10Gd−3Y−1Zn−0.5Zr alloy fabricated by wire-arc directed energy deposition: Phase transformation behavior and mechanical properties [J]. Additive Manufacturing, 2023, 76:103789.

[13] CAO Qian-hui, ZENG Cai-you, QI Bo-jin, JIANG Zi-hao, ZHANG Rui-ze, WANG Fu-de, CONG Bao-qiang. Excellent isotropic mechanical properties of directed energy deposited Mg−Gd−Y−Zr alloys via establishing homogeneous equiaxed grains embedded with dispersed nano-precipitation [J]. Additive Manufacturing, 2023, 67: 103498.

[14] FU Peng-huai, WANG Nan-qing, LIAO Hai-guang, XU Wen-yu, PENG Li-ming, CHEN Juan, HU Guo-qi, DING

Wen-jiang. Microstructure and mechanical properties of high strength Mg−15Gd−1Zn−0.4Zr alloy additive-manufactured by selective laser melting process [J]. Transactions of Nonferrous Metals Society of China, 2021, 31(7): 1969−1978.

[15] GUO Jing, ZHOU Yong, LIU Chang-meng, WU Qian-ru, CHEN Xian-ping, LU Ji-ping. Wire arc additive manufacturing of AZ31 magnesium alloy: grain refinement by adjusting pulse frequency [J]. Materials, 2016, 9: 823.

[16] CAI Xiao-yu, CHEN Fu-kang, DONG Bo-lun, LIN San-bao, YANG Chun-li. Microstructure and mechanical properties of GTA-based wire arc additive manufactured AZ91D magnesium alloy [J]. Journal of Magnesium and Alloys, 2022.

[17] WANG Jie, ZHAO Zhan-yong, BAI Pei-kang, ZHANG Rui-ze, ZHANG Zhen, WANG Li-qing, DU Wen-bo, WANG Fu-de, HUANG Zhi-quan. Microstructure and mechanical properties of AZ31 magnesium alloy prepared using wire arc additive manufacturing [J]. Journal of Alloys and Compounds, 2023, 939: 168665.

[18] ZHANG Zhao-dong, LIU Li-ming, SONG Gang. Welding characteristics of AZ31B magnesium alloy using DC-PMIG welding [J]. Transactions of Nonferrous Metals Society of China, 2013, 23(2): 315−322.

[19] HU Sheng-sun, ZHANG Heng, WANG Zhi-jiang, LIANG Ying, LIU Yong-qiang. The arc characteristics of cold metal transfer welding with AZ31 magnesium alloy wire [J]. Journal of Manufacturing Processes, 2016, 24(1): 298−306.

[20] YUAN T, LUO Z, KOU S. Grain refining of magnesium welds by arc oscillation [J]. Acta Materialia, 2016, 116: 166−176.

[21] WANG Peng, ZHANG Han-zheng, ZHU Hao, LI Qqing-zhuang, FENG Meng-nan. Wire-arc additive manufacturing of AZ31 magnesium alloy fabricated by cold metal transfer heat source: Processing, microstructure, and mechanical behavior [J]. Journal of Materials Processing Technology, 2021, 288: 116895.

[22] ZHANG Heng, HU Sheng-sun, WANG Zhi-jinag, LIANG Ying. The effect of welding speed on microstructures of cold metal transfer deposited AZ31 magnesium alloy clad [J]. Materials & Design, 2015, 86: 894−901.

[23] YANG Xu, LIU Jian-rui, WANG Zhen-nan, LIN Xin, LIU Fen-cheng, HUANG Wei-dong, LIANG En-quan. Microstructure and mechanical properties of wire and arc additive manufactured AZ31 magnesium alloy using cold metal transfer process [J]. Materials Science and Engineering A, 2020, 774: 138942.

[24] CAO Qian-hui, QI Bo-jin, ZENG-Caiyou, ZHANG Rui-ze, HE Bo-chang, QI Ze-wu, WANG Fu-de, WANG Hai-bo, CONG Bao-qiang. Achieving equiaxed microstructure and isotropic mechanical properties of additively manufactured AZ31 magnesium alloy via ultrasonic frequency pulsed arc [J]. Journal of Alloys and Compounds, 2022, 909: 164742.

[25] GUO Yang-yang, QUAN Gao-feng, JIANG Ying-long, REN Ling-bao, FAN Ling-ling, PAN Hou-hong. Formability, microstructure evolution and mechanical properties of wire arc additively manufactured AZ80M magnesium alloy using gas tungsten arc welding [J]. Journal of Magnesium and Alloys, 2021, 9: 192−201.

[26] MA Dong, XU Chun-jie, SUI Shang, TIAN Jun, GUO Can, WU Xiang-quan, ZHANG Zhong-ming, DAN S, SERGEI R. Enhanced strength-ductility synergy in a wire and arc additively manufactured Mg alloy via tuning interlayer dwell time [J]. Journal of Magnesium and Alloys, 2023.

[27] WANG Qi-man, WU Guo-hua, TONG Xin. An investigation into wire arc additive manufacturing of Mg−Y−RE−Zr alloy [J]. Materials Letters, 2022, 326: 132922.

[28] KAH P, SUORANTA R, MARTIKAINEN J. Advanced gas metal arc welding processes [J]. The International Journal of Advanced Manufacturing Technology, 2013, 67: 655−674.

[29] WANG Yong-ji, LI Zhi-yong, ZHANG Ying-qiao, WEI Shou-zheng, YANG Liu-qing, YANG Kang. Segregation in the magnesium/aluminum composites formed by cold arc cladding [J]. Materials Chemistry and Physics, 2021, 266.

[30] WANG Yong-ji, LI Zhi-yong, ZHANG Ying-qiao, WEI Shou-zheng, PEI Xiao-long, YANG Liu-quan. Cold arc cladding of aluminum coatings on AZ61 magnesium alloy: A comparative study [J]. Surface & Coatings Technology, 2019, 375: 442−457.

[31] ZHOU Si-yu, XIE Han, NI Jia-qiang, YANG Guang, QIN Lan-yun, GUO Xinpeng. Metal transfer behavior during CMT-based wire arc additive manufacturing of Ti−6Al−4V alloy [J]. Journal of Manufacturing Processes, 2022, 82: 159−173.

[32] FUJII H, IZUTANI S, MATSUMOTO T, KIGUCHI S, NOGI K. Evaluation of unusual change in contact angle between MgO and molten magnesium [J]. Materials Science and Engineering A, 2006, 417: 99−103.

[33] WAGNER D C, YANG Y K, KOU S. Spatter and porosity in gas-metal arc welding of magnesium alloys: Mechanisms and elimination [J]. Welding Journal, 2013, 92(12): 347−362.

[34] HE Shen, YANG Dong-qing, HUANG Yong, WANG Ke-hong. Effect of the current waveform on the droplet transfer in CMT welding high-nitrogen steel [J]. Journal of Manufacturing Processes, 2022, 75: 41−48.

[35] JIA Yong-hui, HOU Jian, Wang Hang, LE Qi-chi, LAN Qing, CHEN Xing-rui, BAO Lei. Effects of an oscillation electromagnetic field on grain refinement and Al8Mn5 phase formation during direct-chill casting of AZ31B magnesium alloy [J]. Journal of Materials Processing Technology, 2020, 278: 116542.

[36] PAN Fu-sheng, FENG Zhong-xue, ZHANG Xi-yan, TANG Ai-tao. The types and distribution characterization of Al−Mn phases in the AZ61 magnesium alloy [J]. Procedia Engineering, 2012, 27: 833−839.

[37] GUSSEV M N, FIELD K G, BUSBY J T. Deformation localization and dislocation channel dynamics in neutron-irradiated austenitic stainless steels [J]. Journal of Nuclear Materials, 2015, 460: 139−152.

[38] SOMEKAWA H, SINGH A, INOUE T. Enhancement of toughness by grain boundary control in magnesium binary alloys [J]. Materials Science and Engineering A, 2014, 612: 172−178.

[39] ZHANG Zhong-rui, SHEN Jun-qi, BI Ji, HU Sheng-sun, ZHEN Ya-hui, BU Xian-zheng. Microstructure and mechanical properties of weaving wire and arc additive manufactured AZ91 magnesium alloy based on cold metal transfer technique [J]. Materials, 2023, 16(11): 4047.

[40] JATA K V, HOPKINS A K, RIOJA R J. The anisotropy and texture of Al−Li alloys [J]. Materials Science Forum, 1996, 217: 647−652.
[41] BI Ji, SHEN Jun-qi, HU Sheng-sun, ZHEN Ya-hui, YIN Feng-liang, BU Xian-zheng. Microstructure and mechanical properties of AZ91 Mg alloy fabricated by cold metal transfer additive manufacturing [J]. Materials Letters, 2020, 276: 128185.

基于冷弧工艺的电弧增材制造 AZ91 镁合金的工艺、显微组织和力学性能

蔡佰豪[1,2]，范霁康[1,2]，李 杰[1,2]，杨东青[1,2]，彭 勇[1,2]，王克鸿[1,2]

1. 南京理工大学 受控电弧智能增材技术工业和信息化部重点实验室，南京 210094；
2. 南京理工大学 材料科学与工程学院，南京 210094

摘 要：采用基于冷弧工艺的电弧增材制造技术(CA-WAAM)制备具有细小等轴晶粒的 AZ91 镁合金薄壁构件，研究了增材制造过程中的熔滴过渡行为以及增材件的显微组织和力学性能。结果表明，冷弧工艺减少了液桥断裂瞬间产生的飞溅，有效缩短了熔滴过渡周期。沉积试样的显微组织呈现出粗晶和细晶交替分布的层状特征。在逐层沉积过程中，β 相优先沿晶界析出和生长，细小的 η-Al_8Mn_5 相分散在 α-Mg 基体中。增材件的力学性能表现出各向同性的特点，试样垂直方向的极限抗拉强度和伸长率分别为 282.7MPa 和 14.2%；试样硬度分布相对均匀，平均硬度值为 HV 69.6。

关键词：AZ91 镁合金；熔滴过渡；显微组织；力学性能；冷弧工艺

(Edited by Bing YANG)